



ELSEVIER

Contents lists available at ScienceDirect

Mechanics of Materials

journal homepage: www.elsevier.com/locate/mechmat

Research paper

Numerical and experimental analysis of the Young's modulus of cold compacted powder materials



A. Salvadori^{a,b,*}, S. Lee^a, A. Gillman^{a,b}, K. Matouš^{a,b}, C. Shuck^{a,c}, A. Mukasyan^{a,c},
M.T. Beason^{a,d}, I.E. Gunduz^{a,d}, S.F. Son^{a,d}

^a Center for Shock Wave-processing of Advanced Reactive Materials, University of Notre Dame, Notre Dame, Indiana, USA

^b Department of Aerospace and Mechanical Engineering, University of Notre Dame, Notre Dame, Indiana USA

^c Department of Chemical and Biomolecular Engineering, University of Notre Dame, Notre Dame, Indiana, USA

^d School of Mechanical Engineering, Purdue University, West Lafayette, Indiana, USA

ARTICLE INFO

Article history:

Received 28 December 2016

Revised 26 April 2017

Available online 2 June 2017

Keywords:

Young's modulus

Cold compacted metal powders

Image-based modeling

Co-designed experiments and simulations

ABSTRACT

We present co-designed experimental, theoretical, and numerical investigations aiming at estimating the value of the Young's modulus for cold compacted powder materials. The concept of image-based modeling is used to reconstruct the morphology of the powder structure with high fidelity. Analyses on aluminum powder pellets provide significant understanding of the microstructural mechanisms that preside the increase of the elastic properties with compaction. The role of the stress percolation path and its evolution during material densification is highlighted.

© 2017 Elsevier Ltd. All rights reserved.

1. Introduction

Materials or components made from powders have enormous societal and industrial impact. To list some everyday examples: i) pharmaceutical tablets (Michrafy et al., 2002; Kadiri et al., 2005; Wu et al., 2005; Klinzing et al., 2010) are the most widespread use of compressed powder materials; ii) detergent tablets, a mix of surfactants, alkalis, bleaches, and other chemicals, are used in day-to-day chores; iii) candies are often created by compacting glucose powder with a small amount of binder. Structural and advanced materials also take advantage of compression technology. Cold compaction of ceramic powders (Piccolroaz et al., 2006a; 2006b) is extensively used in industry for advanced structural applications, such as chip carriers, and consumer products, such as tiles and porcelain. Powder metallurgy has a broad range of industrial applications, including manufacturing light engineering components and tools, along with bioengineering technologies (Laptev et al., 2016).

In many applications, the manufacturing process begins with cold compaction of powders (Fleck, 1995), performed using dies machined to close tolerances. This methodology enables powder cohesion through mechanical densification, which is governed by different mechanisms, including particle rearrangement, elastic and

plastic deformations. The purpose of compaction is to obtain a green compact, with sufficient strength to withstand further handling operations, such as sintering.

Processing options permit selective placement of phases or pores to achieve targeted effective properties after cold compaction. The mechanical properties of green compacts are strongly influenced by the morphological characteristics of the compound. Micrographs of the particle arrangement show that the morphology of the powder pack changes with the forming pressure from an assembly with ideal point-wise contact to a severely plastically deformed state, with a substantial reduction of voids. This and other studies show that the Young's modulus varies with the stiffness of each phase and with the network of inter-particle contacts.

Tracking the contact regions between the particles while they experience large deformations is a formidably complex task (Gonzalez and Cuitiño, 2016) and is not the goal of this manuscript. This paper aims to estimate the Young's modulus of cold compacted metal powders via computational simulations using *image-based morphological reconstructions* of the microstructure and *high performance computing*. The work has sound motivations: whereas experimental investigations on the topic are covered by relatively broad literature, only a few numerical analyses have been carried out.

Experimental investigations on the elastic properties of cold compacted powders have been published by several authors, see Carnavas and Page (1998) and Argani et al. (2016b) and references therein, studying the effects of the powder morphology. Two major

* Corresponding author.

E-mail address: alberto.salvadori@unibs.it (A. Salvadori).

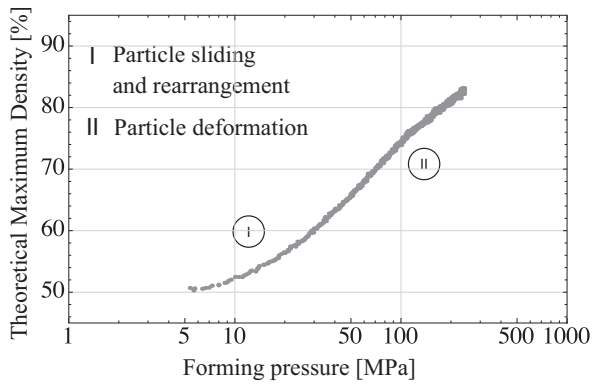


Fig. 1. An illustration of aluminum particle rearrangement, deformation, and densification during compaction. A sharp differentiation between these phases could not be precisely identified. Dots correspond to experimental data, which refer to the same powder compound used for Young's modulus estimation.

conclusions have been confirmed by the present numerical analyses, namely: i) the load response of lightly compressed powders is dominated by its particulate nature and inter-particle forces; ii) the load response of heavily compressed materials is similar to that of a porous solid. Our simulations provide further insight into the microstructural mechanisms that control the increase of the Young's modulus with forming pressure by highlighting the relevance of the stress percolation path generated by the contact areas between particles. Similar studies have been made by [Kruyt \(2016\)](#) and [Kruyt and Antony \(2007\)](#), as well as by [Poquillon et al. \(2002a; 2002b\)](#). The role of the rate of compaction was investigated more recently in [Wang et al. \(2009\)](#).

Literature on macroscopic models of metal powder densification under cold compaction is very broad (cf. [Gu et al., 2001](#) and the references in [Piccolroaz et al. \(2006a\)](#)). Microscopic investigations have been carried out by studying the contact force distribution in idealized rigid ([Kanatani, 1981](#)) or deformable ([Jefferson et al., 2002](#); [Argani et al., 2016a](#)) particles. Numerical analyses have been performed by the discrete ([Makse et al., 2000](#)) or finite ([Argani et al., 2016a](#); [Kim and Cho, 2001](#); [Lee and Kim, 2002](#)) element methods. By treating the powder material as a two-phase composite, effective properties can be extracted from the extensive literature on the subject - see for instance [Torquato \(2002\)](#). Numerical investigations in the present paper have been compared to the Hashin-Shtrickman bounds ([Hashin and Shtrickman, 1962](#)) and the boolean model of spheres ([Serra, 1980](#); [Stoyan and Mecke, 2005](#)) - also termed overlapping spheres theory ([Torquato, 1997; 1998](#)).

Computational simulations have the capability to test virtual materials, allowing for major cost savings, provided that scientific predictivity is achieved. The present work pinpoints the rel-

evance of the image-based strategy in this regard. It confirms insightful conclusions drawn on experimental basis about the micro-mechanics of the cold compaction by highlighting the role of morphology and its evolution during the forming process. Specifically, it brings attention to the fact that a unique value for the Young's modulus, especially at low volume fractions, may not be identified since it is severely influenced by the history of deformation and the generation of the stress percolation path ([Radjai et al., 1998](#)).

The paper is organized as follows. [Section 2](#) comprises the Young's modulus measurements, as well as the full description of the powder compound and of the experimental setup. The notion of *image-based modeling* is discussed in the subsequent section, highlighting the fundamental tasks of data acquisition, the construction of percolation paths, and the statistical and the numerical analyses. Results are discussed in [Section 4](#), assessing numerically several insights provided on experimental basis.

2. Experimental evidence

Powders (99.8% pure Al with -100+325 and -325 mesh size) have been purchased from Alfa Aesar. They have been sieved for 24 h using a sieve shaker (RO-TAP RX-29) to a particle size range of 106–355 μm . Young's modulus has been measured from the sieved as-received and high-energy ball milled Al powders. The milling procedure and results for high-energy ball milled Al powders are reported in [Appendix A](#).

2.1. Quasi-static measurement of Young's modulus

Pellets ranging from 80 to 98% theoretical maximum density (TMD) were cold pressed from the sieved Al powders in a 6.35 mm die purchased from MTI Corporation at a 1:1 aspect ratio. By increasing the amount of forming pressure, powder materials were transformed from a granular to a dense state in different phases, which have been plotted in [Fig. 1](#).

The faces of the pellets were sanded to a flatness of approximately 10 μm . The samples were then loaded in 300 N/step increments in a uniaxial configuration, shown in [Fig. 2](#). Graphite powder was used between the steel platens and the compact surface to reduce the effect of friction. The changes in the height of the pellets were measured using an Epsilon 3542 Axial Extensometer attached to the platens above and below the samples with the signal being recorded on a Tektronix 3054b oscilloscope. The relative density of the pellets was calculated after the experiment by measuring the pellet height, diameter, and mass.

The total measured displacement, δx_{tot} , is the sum of the displacement due to the measured portion of the plates, δx_{sys} , and of the sample, δx . Combining Hooke's law ($\sigma = E\varepsilon$) with the definition of engineering strain ($\varepsilon = \delta x/L$) and engineering stress ($\sigma = P/A$), the displacement due to the deformation of the sample is

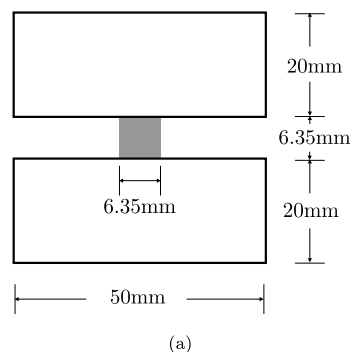


Fig. 2. Experimental setup for uniaxial compression experiments.

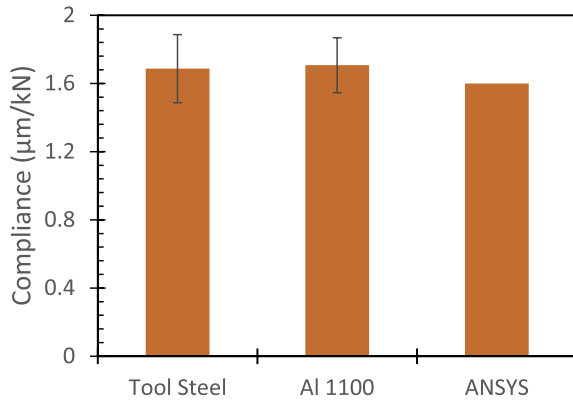


Fig. 3. Comparison of experimentally measured compliance data to ANSYS calculation.

given by $\delta x = PL/E\sigma$, where σ is the axial stress, E is the Young's modulus, ε is the axial strain, P is the axial load, L is the initial sample height, and A is the initial cross-sectional area of the sample. With a test material of known Young's modulus, E^* , and cross-sectional area, A^* , the displacement due to the platens is calculated from $\delta x_{\text{sys}} = \delta x_{\text{tot}} - PL/E^*A^*$. Tool steel and aluminum rods of the same diameter as the pellets were used to measure the system compliance, C . The value of C was determined by loading the materials under five different loading conditions and calculating the system displacement. Once calculated, a linear fit of the load versus system displacement provides the compliance. The resulting compliance can be seen in Fig. 3.

The system compliance was estimated also through a linear elastic simulation using the commercial package ANSYS. In this simulation, a single platen was modeled with a uniform pressure across a 6.35 mm circular area in the center of the platen. The base of the platen was fixed. The total displacement for a single platen was measured at the center of the loading area. Plotting a linear fit between load and twice the displacement of a single platen yielded the result seen in Fig. 3. The measured response matches the elastic calculation using ANSYS well.

Data generated from the above experiments are plotted in Fig. 4. The pellets were loaded to the peak at a rate of ~ 1 kN/s, held at this load for a period of approximately 6 s, and then released to a lower level where it was held for another 6 s period. All strain measurements were taken upon release. This was continued until the load was completely released (4–5 steps). This allowed very accurate measurement of the position by averaging the voltage signal over a 6 s period. This process was repeated 3 times on each pellet. Fig. 5 depicts the Young's modulus estimated from

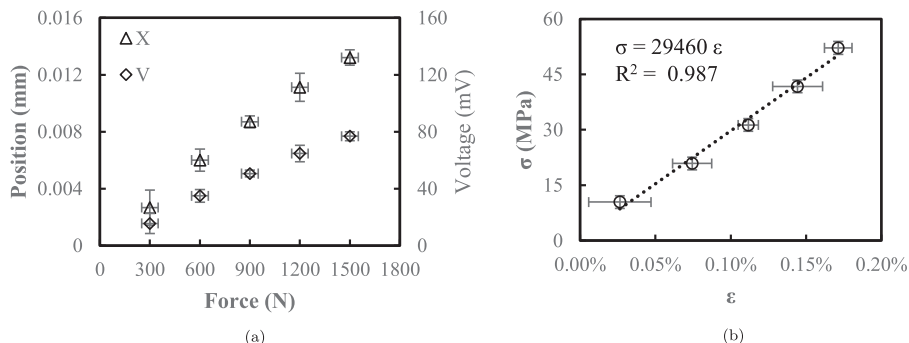


Fig. 4. Data generated from uniaxial strain measurement. (a) Position and voltage data with error bars on position representing 2 standard deviations; (b) $\sigma - \varepsilon$ data with error bars propagated from uncertainty in voltage and axial force.

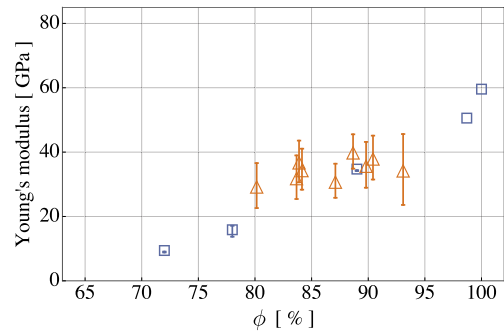


Fig. 5. Young's modulus obtained from experimental measurements. Compounds have been measured quasi-statically (unfilled triangles) as well as dynamically (unfilled squares). Error bars represent twice the standard deviation.

experimental measurements. Unfortunately, it was not possible to measure the quasi-static Young's modulus at any volume fraction (denoted henceforth with ϕ) below 80% TMD, because the cold-pressed pellets were too fragile to handle at those densities.

2.2. Dynamic Young's modulus

Specimens of elastic materials at ambient temperatures possess specific mechanical resonant frequencies, which are determined by the elastic modulus, mass, and geometry of the test specimen. Experimental tests by impulse excitation, according to ASTM E 1876 standard, measure the fundamental resonant frequency of disc-shaped specimens by exciting them mechanically with a singular elastic strike with an impulse tool. A transducer senses the resulting mechanical vibrations of the specimen and transforms them into electric signals. The supports of the specimens, the impulse locations, and the signal pick-up points are selected to induce and measure specific modes of the transient vibrations. The signals are analyzed and the fundamental resonant frequency is measured. The Poisson's ratio is determined using the resonant frequencies of the first two natural vibration modes. The dynamic Young's modulus and dynamic shear modulus are then calculated using the Poisson's ratio, the experimentally-determined fundamental resonant frequencies, and the specimen dimensions and mass.

Dynamic Young's modulus experimental tests have been carried out on -100+325 aluminum powders at 99.8% purity, sieved to the 106–355 μm size range over 24 h. The aluminum powder was cold pressed to disk samples (30 mm in diameter and between 2.3 – 2.9 mm in height) with TMD varying from 70% to 100%. For each TMD, two separate samples were prepared, and each sample

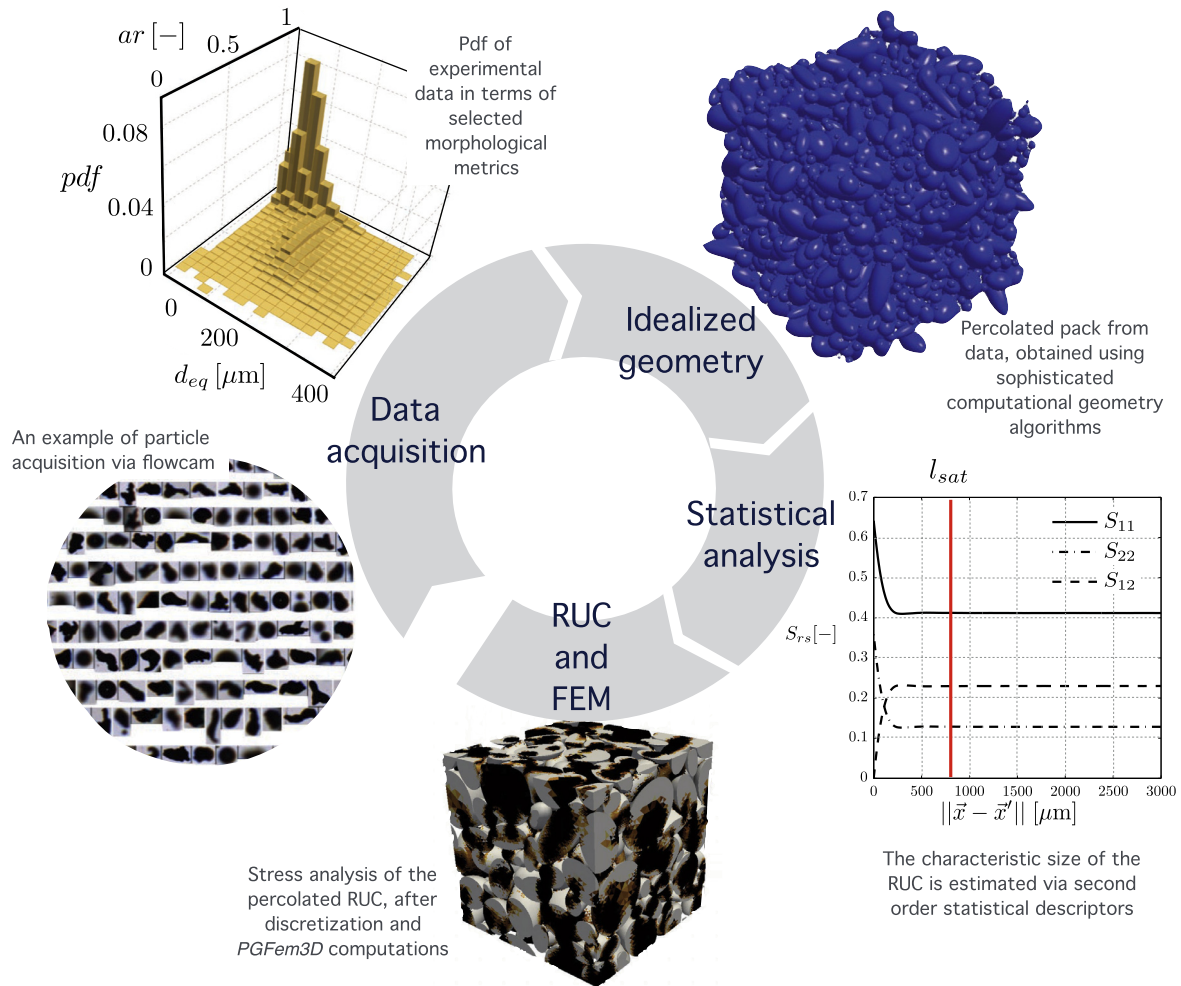


Fig. 6. A pictorial view of the I-BM concept. The probability density function of a very large number of particles is recovered after experimental data acquisition, in terms of morphological features (shapes, sizes, and aspect ratio). The 3D geometry of a large pack of particles has been replicated by an in-house developed software that makes use of complex packing algorithms and sophisticated computational geometry tools to build the percolation path required by the porous nature of powder pellets. A statistical analysis is carried out afterwards in order to identify the characteristic size of the RUC, which has been estimated by a two point probability function analysis. The RUC is finally discretized by finite elements, towards numerical simulations.

was tested three times.¹ Outcomes are compared with quasi-static Young's modulus in Fig. 5.

Dynamic Young's modulus experimental tests by impulse excitation are specifically appropriate for materials that are elastic, homogeneous, and isotropic (E1876-01, 2002). According to the ASTM E 1876 standard, this method of determining the moduli is applicable to composite and inhomogeneous materials only with careful consideration of the effect of inhomogeneities. The influence of the morphology on the impulse wave propagation and resonant frequency in the specimens has a direct effect on the effective elastic properties of each specimen.

Comparisons between quasi-static and dynamic Young's modulus as a function of the TMD (see Fig. 5) show a similar trend, yet suggest that the dynamic Young's modulus is lower than the quasi-static one at small volume fractions, and thus high porosity.

3. Image-based modeling

Image-based modeling (I-BM) of particulate composite materials can be defined as the class of computational algorithms and ex-

perimental methods that allow for reconstruction of the morphology of an ensemble, accounting for the fine structure properties of the particles (Matouš et al., 2017). I-BM encompasses four fundamental tasks: *data acquisition*, *statistical analysis* of the particulate pack, *computational domain reconstruction* of the representative unit cell (RUC) to match selected statistical descriptors measured from real image data, and *computational modeling*. This procedure will be detailed with reference to the aluminum powders described in Section 2. Fig. 6 visually depicts the I-BM concept.

3.1. Data acquisition

Morphological data of a powder compound can be acquired with different techniques, either destructive or not, depending upon the size of the microstructure and the resolution required by the investigation (Shuck et al., 2016). Tomography, for instance, can be used to reconstruct three-dimensional packs *in situ*, and image-processing afterwards provides data-sets of idealized shapes that reproduce the actual powder compound (Gillman et al., 2013). Micro-computed tomography (micro-CT) was used in several contexts (solid propellant, glass bead, paper, sandstones, engineered cementitious composites) and microtomographic data have been

¹ Measurements were provided by IMCE, Genk, Belgium.

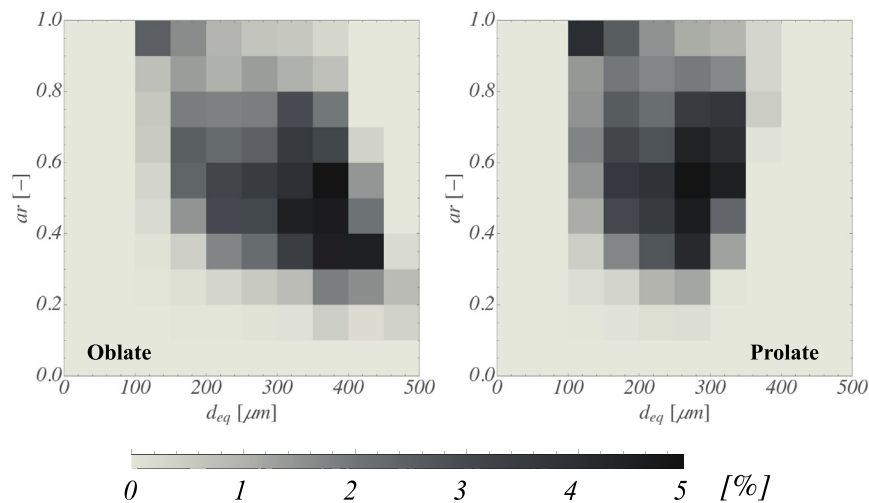


Fig. 7. Volume-based distributions (in percentage of the total particles volume) plotted as a function of the aspect ratio (ar) and of the equivalent diameter (d_{eq}) for oblate and prolate sets of particles on a 10×10 grid.

analyzed in Gillman et al. (2013) and Lee et al. (2011) with some similarities to the present note. Since traditional X-ray systems do not penetrate metals easily, micro-CT was not used in this scientific endeavor.

Instead, characterization of the particle geometry was conducted using a FlowCam® (Fluid Imaging Technologies, USA) system. This method of analysis was chosen due to the high throughput of individual particles. 2.5 g of aluminum powders were initially suspended in 500 mL of a 5% polyvinylpyrrolidone-deionized water solution, then sonicated for 30 min. The suspension of powders was flown through a 1 mL cell with a corresponding optical microscope (the optics were 4x for the microscope lens). Each particle that flowed in the field of view was individually imaged and processed with the VisualSpreadsheet software for size and shape characteristics.

Acquired data were analyzed in order to computationally reconstruct the morphology of the three-dimensional powder pack from the list of geometrical properties available after the acquisition.

The FlowCam® technique provides a two-dimensional projection of each particle,² sampled as an ellipse of semi-axes a and b . Particles have been further idealized as three-dimensional ellipsoids, with third semi-axis of length c . Two data sets have been generated concurrently in order to estimate the amount of c , assuming that particles are either all *oblate*, i.e. $a = c > b$, or all *prolate*, i.e. $a > b = c$.

Rectangular domains, in the aspect ratio (ar) and diameter of an equivalent spherical particle (d_{eq}), have been discretized by an $N \times N$ grid. All particles that pertain to any of the N^2 subdomains have been associated to a single representative particle with the equivalent diameter and aspect ratio of the centroid of the subdomain. The volume distributions on a 10×10 grid are plotted as a function of the aspect ratio (ar) and of the equivalent diameter (d_{eq}) in Fig. 7.

² FlowCam® allows acquiring large sets of particles image data for analysis. Samples are put into the flow cell in the optical path. As the sample passes, a flash LED is triggered behind the flow cell which backlights the sample and effectively freezes the particles in motion. Simultaneous to the flash, the computer instructs the camera viewing the sample through the microscope optics to acquire frame of the flow cell view illuminated by the flash. When each frame reaches the computer, the software automatically extracts separate images of each particle for further processing. Each image and several related measurements are stored for each particle. The area of the projected image is used in subsequent calculations of the area-equivalent diameter. Lengths of the major and minor axes of a Legendre ellipse, whose center is the centroid of the particle shape, are measured. The moments of the Legendre

Fig. 8 depicts the distribution of oblate particles on a 10×10 grid. A similar plot results for prolate particles, also. The distribution is plotted against the equivalent diameter of idealized particles in the range [100, 500] microns. Curve I represents the normalized number of particles, the dashed curve II is the normalized volume of particles, curve III is the cumulative volume of all acquired particles, and finally the dots represent the volume estimated from the 10×10 discretization of experimental data. Stemming from the 100 idealized representatives, and on the volume-based distributions in Fig. 7, a set of 19 oblate and 18 prolate bins was selected. Based on this data, we have generated a large pack (see Fig. 6 top right) that contains 992 particles, 424 oblate and 568 prolate particles respectively. This microstructure has been packed in a cube of size 1.731 mm, at 65, 70 and 75% volume fraction using the particle packing software *Rocpack* (Maggi et al., 2008; Stafford and Jackson, 2010).

Rocpack is based on a hybrid algorithm combining the optimal features of the Lubachevsky-Stillinger and Adaptive Shrinking Cell algorithms, which begins by placing the 992 particles with zero initial volume (points) at random locations inside the domain of interest. The particles are given random velocities, sampled from a Maxwell-Boltzmann distribution, and are allowed to grow at a specified growth rate. The particles collide and rearrange as they grow to fill the space in the domain. The algorithm stops when the specified densities of 65%, 70%, and 75% are reached. For an extensive description of *Rocpack*, the reader may refer to Stafford and Jackson (2010) and Amadio (2014).

3.2. Percolation path construction

Since the packing algorithm does not provide interconnections, computational geometry algorithms have been devised in order to construct percolation paths. The two closest points between two ellipsoids are sought first: they define the distance between the particles. In the midpoint of these two locations a joint, typically in the form of a sphere, is inserted if the distance between particles is below a given constant, termed *zero-distance parameter*. Accordingly, two parameters define the percolation path: the radius of the spherical interconnection and the minimum distance between two particles in order to consider them as connected (the zero-distance

ellipse and shape are the same up to the second order. The aspect ratio is obtained by dividing the minor axis by the major axis.

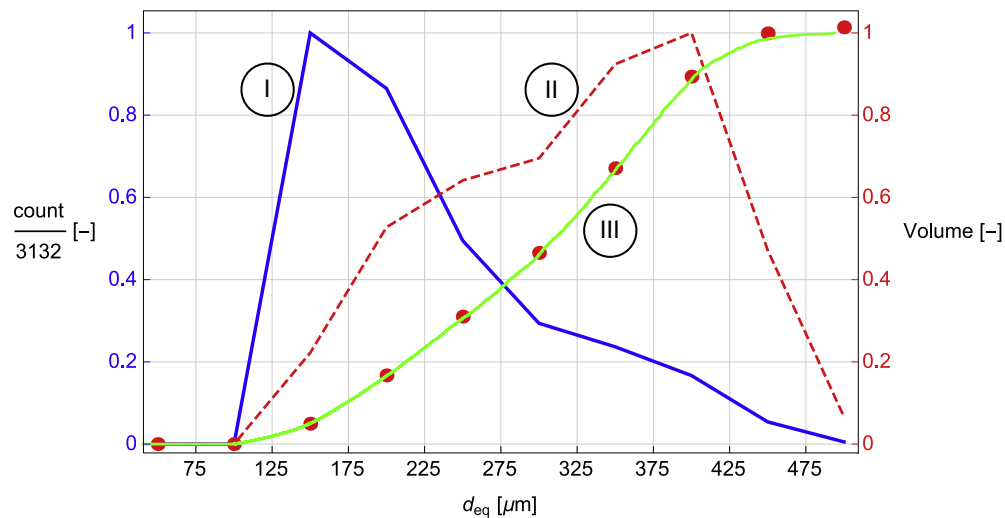


Fig. 8. Oblate particle set distribution on a 10×10 grid, depicted in terms of equivalent diameter in the range [100, 500] microns. Curve I represents the normalized number of particles, curve II the normalized volume of particles, curve III the cumulative volume of all acquired particles, the dots the volume estimated from the 10×10 discretization of Fig. 7.

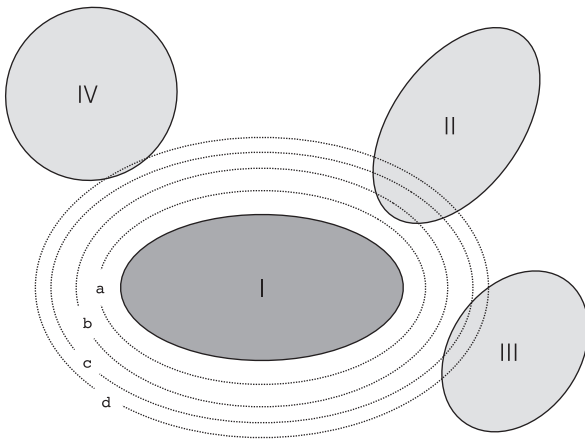


Fig. 9. Influence of the zero-distance parameter on the number of interconnections. For the distance a of the zero-distance parameter, no particles are connected. For the amount b , two particles are joined, whereas three (four) particles are joined for the amount c (d).

parameter). Thus, the increment of volume fraction and the surface area of the interconnections depends upon these two parameters.

The number of joints is influenced by the zero-distance parameter: the larger this parameter, the larger the number of linked particles. At the same time, the zero-distance parameter also influences the connectivity of the pack: the smaller the zero-distance parameter the higher the number of particles that are disconnected and “float” in the Euclidean space.³ Fig. 9 describes how the zero-distance parameter influences the number of interconnections and illustrates that the zero-distance parameter is the lower bound of the radius of the joints, such that a spherical joint itself is not a disconnected entity. The surface area of the interconnections is related to the radius of the joint, see Fig. 10. This notion may require an accurate topological definition, yet here it is taken as the area of the largest circle within the spherical joint radius.

The goal of spherical connections is primarily to simulate the “pointwise” contact between particles. Accordingly, the increment of volume due to the joints must be small compared to the par-

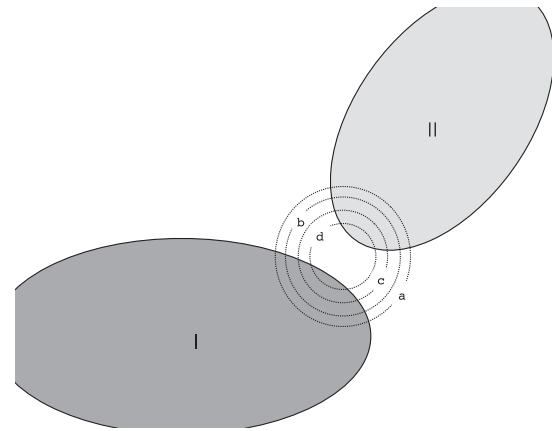


Fig. 10. Influence of the radius of the spherical joint on the surface area of the interconnections, which can be estimated by the intersection between the circles ($a - d$) and the elliptical boundary of particles ($I - II$).

tle’s volume. Nevertheless, increasing the radius of the spherical interconnection may lead to a significant overlap between particles and may substantially increment the volume fraction of the RUC. How this affects the Young’s modulus will be discussed in Section 4.

In reality, plastic deformation during cold compaction may increase the number of contact locations as well as their surface area. This effect is particularly significant during the final part of the compaction process of a metallic powder - see Fig. 1. To simulate this occurrence, one may consider to enlarge the particles rather than adding connections between them. By increasing the particle size, however, volume is generated not just at the closest point location, but over the whole pack - see Fig. 11. Therefore, the volume fraction increases more significantly than the surface area, in a “global” fashion that does not appear to reproduce properly the evolution of the particle shape during compaction. Therefore, we simulate particle contact by local joint addition and growth.

3.3. Statistical micro-mechanics concepts

For materials that satisfy ergodicity, statistical homogeneity, and isotropy the one- and two-point probability functions can be

³ Full connectivity between the particles in the RUCs is ensured in the numerical analyses in Section 3.4.

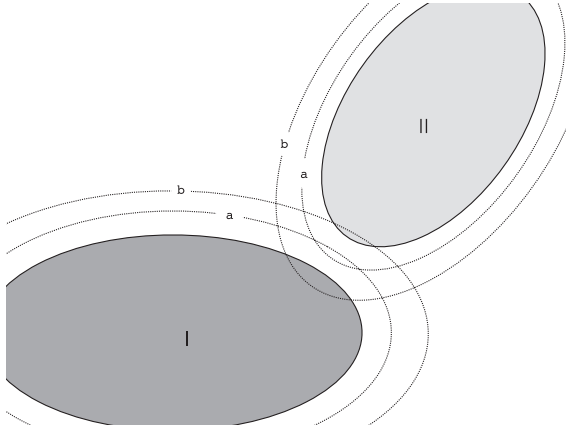


Fig. 11. Overlapping while the particles undergo a homothetic transformation.

defined as follows:

$$c_r = \int_V \chi_r(\vec{x}) dV, \quad S_{rs}(\|\vec{d}\|) = \int_V \chi_r(\vec{x}) \chi_s(\vec{x} + \vec{d}) dV_x. \quad (1)$$

Here $\chi_r(\vec{x})$ is the phase r indicator function, which holds 1 if point \vec{x} is in phase r and zero otherwise. c_r is the volume fraction of the phase r . Functions S_{rs} represent the probability of the endpoints \vec{x} and $\vec{y} = \vec{x} + \vec{d}$ of a line of length $\|\vec{d}\|$ existing in both phases r (for \vec{x}) and s (for \vec{y}) simultaneously. To evaluate S_{rs} all orientations of the line in 3D space have been averaged. Details on the numerical evaluation can be found in Lee et al. (2009) and Collins et al. (2010).

Statistical micro-mechanics theories that include higher order statistical measures (such as one, two, and three-point probability functions) have been shown to yield accurate predictions of effective material properties (Roberts and Garboczi, 2002; Pham and Torquato, 2003; Gillman and Matouš, 2014; Gillman et al., 2015). A third-order estimate of the elastic stiffness tensor derived by Torquato (1997; 1998) is considered in Section 4 for comparison with numerical and experimental analyses. The three-point approximation for the effective bulk (K_e) and shear (G_e) modulus of bicontinuous porous media reads

$$\frac{K_e}{K_1} = \frac{1 + \frac{4G_1}{3K_1}K_{21}c_2 - \frac{10G_1}{3K_1 + 6G_1}K_{21}G_{21}c_1\zeta_2}{1 - K_{21}c_2 - \frac{10G_1}{3K_1 + 6G_1}K_{21}G_{21}c_1\zeta_2}, \quad (2a)$$

and

$$\frac{G_e}{G_1} = \frac{1 + \frac{9K_1 + 8G_1}{6K_1 + 12G_1}G_{21}c_2 - \frac{2K_{21}G_{21}G_1}{3K_1 + 6G_1}c_1\zeta_2 \dots - \frac{G_{21}^2}{6} \left\{ \left[\frac{3K_1 + G_1}{K_1 + 2G_1} \right]^2 c_1\eta_2 + 5G_1 \left[\frac{2K_1 + 3G_1}{(K_1 + 2G_1)^2} \right] c_1\zeta_2 \right\}}{1 - G_{21}c_2 - \frac{2K_{21}G_{21}G_1}{3K_1 + 6G_1}c_1\zeta_2 \dots - \frac{G_{21}^2}{6} \left\{ \left[\frac{3K_1 + G_1}{K_1 + 2G_1} \right]^2 c_1\eta_2 + 5G_1 \left[\frac{2K_1 + 3G_1}{(K_1 + 2G_1)^2} \right] c_1\zeta_2 \right\}}, \quad (2b)$$

where

$$K_{21} = \frac{K_2 - K_1}{K_2 + \frac{4}{3}G_1}, \quad G_{21} = \frac{G_2 - G_1}{G_2 + G_1 \frac{9K_1 + 8G_1}{6K_1 + 12G_1}}. \quad (2c)$$

Here, K_q and G_q are the bulk and shear moduli of phase q , respectively. Phase $q = 1$ represents the solid particles, and $q = 2$ identifies the void phase.

The detailed mathematical theories for deriving effective material properties while incorporating a high-order statistical description of the microstructure can be found, for instance, in books by Milton (2002) and Torquato (2002). In the latter, the interested reader can find formulae (20.67) and (20.171) for the microstructural parameters ζ_2 and η_2 used in Eqs. (2a) and (2b). We do not reprint these parameters here for the sake of brevity, but note that ζ_2 and η_2 are functions of the one-, two-point probability functions (see formula (1)) as well as of the three-point probability function, which vary for different microstructures. In Section 4, we will compare numerical simulations to the microstructural boolean model of spheres (for which the n -point probability functions are formulated analytically) using accurate data published in Helte (1995).

3.4. Numerical analysis

The saturation point l_{sat} of the two-point probability functions in Eq. (1) yields a geometrical length scale, $l_{RUC} \approx 2l_{sat}$, which has been shown (Torquato, 2002) to define the smallest cubic sample that can statistically describe the powder compound (up to the second order). The saturation point l_{sat} is the size at which the first derivative of all isotropic two-point probability functions vanish (numerically, their absolute value is below an assigned tolerance) (Lee et al., 2009). Fig. 12 clearly depicts this concept for the aluminum powders analyzed in the present study: the functions saturate around $l_{sat} = 400 \mu\text{m}$, and thus suggest a RUC side length of $l_{RUC} \geq 800 \mu\text{m}$.

Five realizations of RUCs at 65%, 70%, and 75% volume fraction have been generated considering joints of radius of $21.4 \mu\text{m}$. To this aim, the particle packing software *Rocpack* (Maggi et al., 2008) was used to generate the fifteen RUCs, five for each volume fraction set, each of size $l_{RUC} \geq 800 \mu\text{m}$ according to the I-BM concept with full connectivity of the particles. Fig. 13 shows the geometry of one of the RUCs at different volume fractions.

The connected set of ellipsoidal particles and spherical joints has been discretized afterwards, using the 3D mesh generator *Netgen*.⁴ This tool natively implements three-dimensional primitives (spheres, ellipsoids, boxes) and boolean operations between them, and provides tetrahedral element meshes. Numerical analyses of the five RUC realizations, considering different mesh refinements, allowed for the statistical characterization of the Young's modulus estimation.

Finite elements simulations stem from the weak form of the governing equations, which are the balance of linear and angular momentum together with the constitutive specifications. With reference to the latter, the assumption is made that the intrinsic shear (G) and bulk (K) moduli in the particles do not change with the forming pressure,⁵ whereas the effective properties of the compound obviously will. The isochoric-volumetric decoupling of the strain energy function W

$$W(\mathbf{C}, \mathbf{J}) = \hat{W}(\hat{\mathbf{C}}) + U(\mathbf{J}), \quad (3)$$

is applied (Doll and Schweizerhof, 2000). In Eq. (3), \mathbf{J} is the determinant of the deformation gradient \mathbf{F} , $\mathbf{C} = \mathbf{F}^T \mathbf{F}$ is the right Cauchy–Green deformation tensor, and $\hat{\mathbf{C}} = \mathbf{J}^{-2/3} \mathbf{C}$ is its isochoric counterpart. The isochoric strain energy function \hat{W} has been taken as for a neoHookean material model

$$\hat{W}(\hat{\mathbf{C}}) = \frac{G}{2} (\text{tr}[\hat{\mathbf{C}}] - 3), \quad (4)$$

⁴ NETGEN is open source based on the LGPL license. NETGEN has been developed at RWTH Aachen University, Germany and Johannes Kepler University Linz, Austria.

⁵ Shear $G = 26 \text{ GPa}$ and bulk $K = 76 \text{ GPa}$ moduli have been taken from literature for pure aluminum.

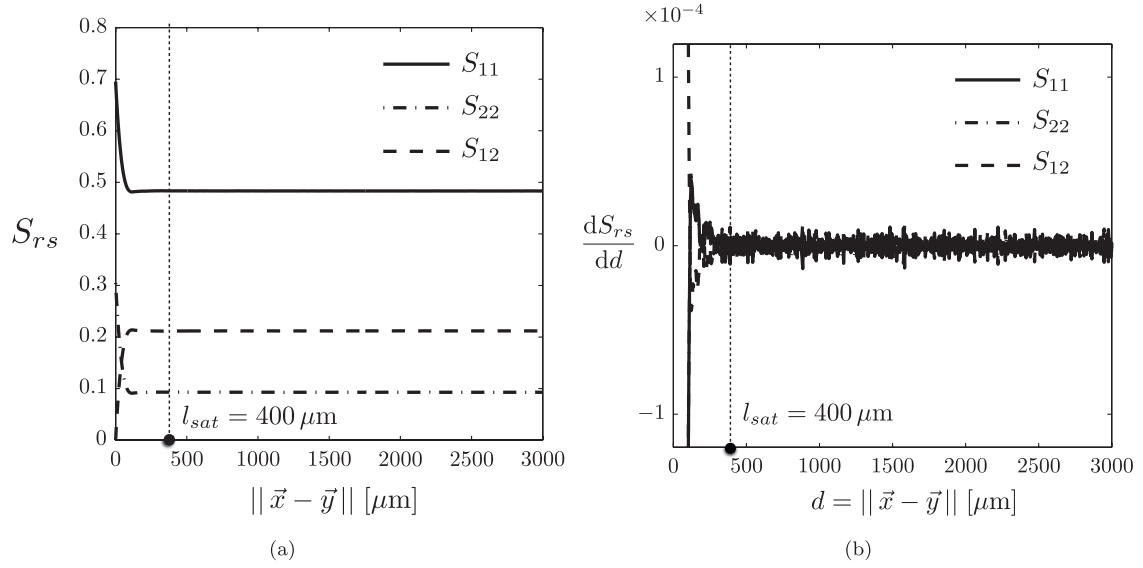


Fig. 12. Two-point probability functions for the aluminum powder, $\phi = 75\%$, subject of the present study.

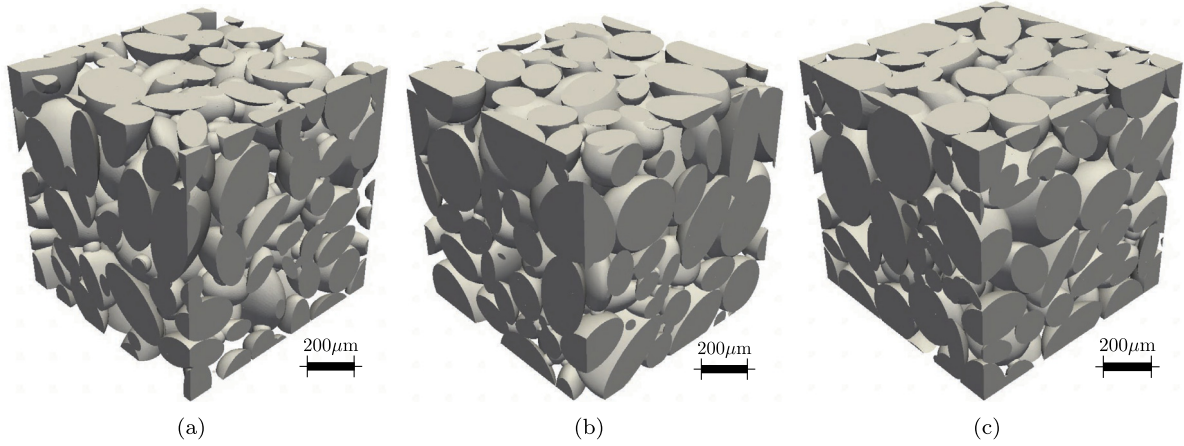


Fig. 13. Percolated particle RUCs at 65% volume fraction (a), 70% (b), and 75% (c) constructed as detailed in Section 3 and corresponding to the particles distribution of Fig. 7. The joint radius is 21.4 μm . All RUCs contain 53 oblate and 71 prolate particles, selected on a set of 19 oblate bins and 18 prolate bins according to the volume based distribution of Fig. 7. The size of the RUC for $\phi=65\%$ is 887 μm , for $\phi=70\%$ is 865 μm , and for $\phi=75\%$ is 849 μm .

whereas the volumetric contribution holds (Doll and Schweizerhof, 2000)

$$U(J) = \frac{K}{2} (J - 1) \ln J. \quad (5)$$

The RUCs have been subject to loading conditions that reproduce the experimental setup described in Section 2. One of the six faces of the cubic RUC has been fully constrained in its normal direction, and let free to expand (frictionless) in any tangential direction. The opposite face has been displacement controlled, by imposing a constant displacement rate. Free expansion has been allowed on the other four faces.

Simulations have been performed with a highly parallel in-house package, *PGFem3D* (Mosby and Matouš, 2015; 2016). No inertia effects have been accounted for. Finite element analyses provide reaction forces as the integral of the pressures on the constrained faces. Those reaction forces are the counterpart of the experimentally measured forces. Effective Young's modulus has been evaluated as the ratio between the engineering stress (estimated on the area of the RUC face) and the engineering strain. Fig. 14 plots the estimated values as a function of the volume fraction for joints with a radius of 21.4 μm . Error bars, which represent twice the standard deviation of 5 RUC realizations, show that the

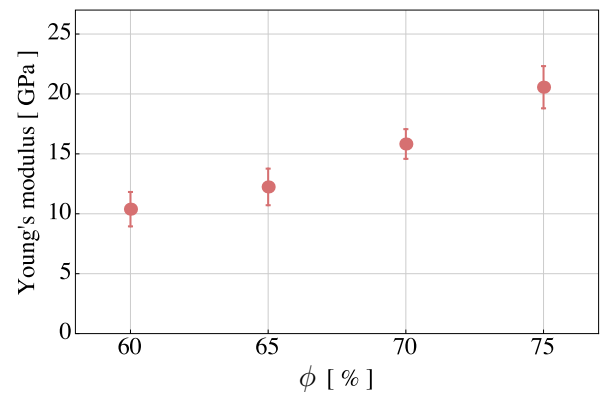


Fig. 14. Young's modulus of cold compacted Al powder via image-based modeling and simulations for joints with a radius of 21.4 μm . Error bars represent twice the standard deviation of 5 RUC realizations.

standard deviation in numerical analysis is significantly smaller than in experimental investigations (see Fig. 5). Stemming from the accuracy of the numerical solution, only one single RUC realization

Table 1

Young's modulus (E) evolution with the surface area of the interconnecting network, as a function of the joint radius, at point-wise connected volume fraction about 75%. Radii below 21.4 μm increase the volume fraction by an amount less than 0.5%, thus simulating the rearrangement mechanism.

Label on Fig. 16	Joint					Discrete ϕ [-]	E [GPa]
	radius [μm]	#	surf. area [μm^2]	surf. area [%]	vol. [%]		
A	5.9	44	6.9e3	3.3e-2	0.0048	0.7425	19.5
B	12.7	64	3.2e4	0.23	0.034	0.7427	20.5
C	21.4	117	1.7e5	1.19	0.49	0.7461	21.7
D	32.2	205	6.6e5	4.70	3.21	0.766	24.9
E	42.9	242	1.4e6	9.87	6.47	0.790	28.3
F	47.9	343	2.5e6	17.5	12.06	0.832	34.7
G	52.5	378	3.3e6	23.12	15.01	0.854	38.8

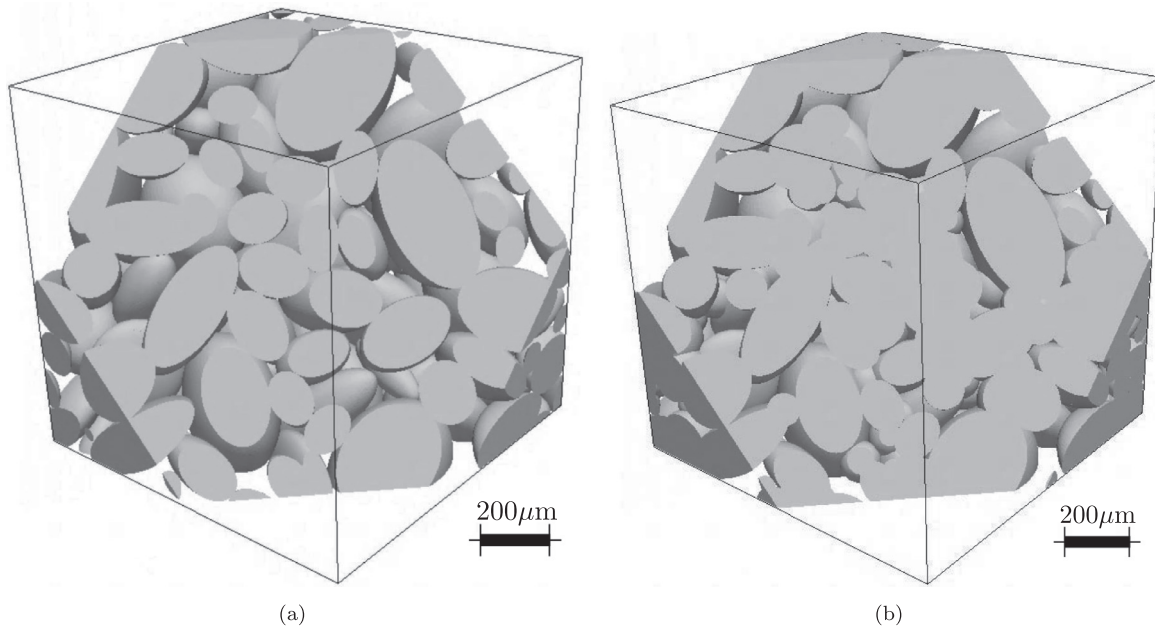


Fig. 15. A clip of the particulate pack at 75% volume fraction with 5.9 μm joints (a) and with 52.5 μm joints (b).

at 65, 70, and 75% volume fraction has been considered in all simulations that follows. The influence of the joint size on the Young's modulus has been studied and will be discussed in the next section.

4. Discussion

The effective mechanical properties of cold compacted powders are strongly influenced by the morphology of the arrangement, in a non trivial way that depends significantly on the micro-structural interactions between the particles and on their ability to distribute the stress field through the volume. The number and size of interconnections between the particles in cold compressed metal powders evolve with the forming pressure, increasing the ability of the powder compound to transfer the force and in turn the effective stiffness of the material. As the area of interconnections saturates while the volume fraction tends to unity, so does the effective Young's modulus towards an experimentally measured value that corresponds to the intrinsic, solid aluminum Young's modulus, as depicted in Fig. 5.

Analysis for compounds at 75% volume fraction - Table 1 depicts the influence of the surface area of the interconnecting network on the Young's modulus for a RUC at 75% volume fraction. Several radii of spherical connections have been selected. The largest radius, 52.5 μm , is about a half of the smallest axis of the smallest particle (106 μm). The smallest radius is 5.9 μm . Two clips of the reconstructed particle packs can be seen in Fig. 15.

The zero-distance parameter was enlarged together with the size of the joints⁶; the number of connected particles therefore grew by about a factor 8.5, as reported in the third column of Table 1. At the initial stage (points A-C in Table 1), the surface area increased significantly, by one order of magnitude per each radius increment - see column 4, and so did the volume added to the particle pack. However, the increment in volume stayed below 0.5% for a joint radius less than or equal to 21.4 μm . Column 5 reports the ratio between surface area of the joints and the total surface area of the particles, whereas column 6 shows the ratio between the added volume and the volume of the particles alone after the discretization, which amounts to 0.456 mm^3 .

Carnavas and Page (Carnavas and Page, 1998) noticed in their experimental investigations that the load response of lightly compressed powders is dominated by its particulate nature and inter-particle forces. The experimental and numerical analyses in this paper completely support this statement. Simulations have been run first by constructing the percolation path via small spherical joints, which adequately simulate a *particle rearrangement with point-wise inter-particle force transmission*. Relevant outcomes have been plotted in Fig. 16 at points A, B, and C. They correspond to joint radius less or equal than 21.4 μm .⁷ The boolean model

⁶ In the spirit of the present work, the zero-distance parameter captures the rise of the plastic deformation due to cold compaction.

⁷ See the first three lines of Tables 1 and 2.

Table 2

Young's modulus (E) evolution with the surface area of the interconnecting network, as a function of the joint radius, at volume fraction 70%.

Label on Fig. 16	Joint			Discrete			E [GPa]
	radius [μm]	#	surf. area [μm^2]	surf. area [%]	vol. [%]	ϕ [-]	
I	5.9	68	7.6e3	5.45e-2	0.0072	0.6943	12.8
-	12.7	109	5.7e4	0.407	0.0737	0.6947	14.2
-	21.4	175	2.6e5	1.87	0.665	0.699	16.7
-	32.2	253	8.5e5	6.08	3.33	0.717	20.3
H	42.9	323	1.9e6	13.8	8.03	0.750	26.2

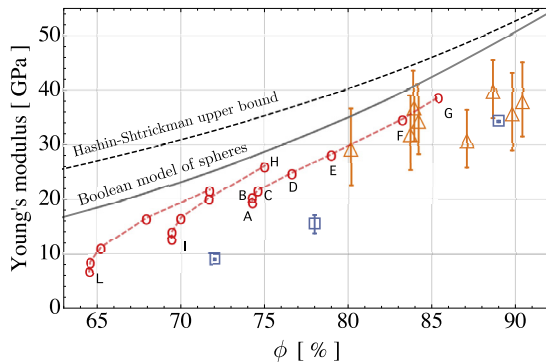


Fig. 16. Young's modulus estimation. Image-based simulations (circular empty markers) are compared with quasi-static experimental analysis (triangular empty markers with error bars) as well as with the Boolean model of spheres curve (see equations (2), printed in continuous line) and the Hashin-Shtrickman bound (dashed line). Square markers are relevant to dynamic Young's modulus experimental outcomes. Error bars represent twice the standard deviation.

of spheres theory over-estimates the Young's modulus by 30% or more, while the Hashin-Shtrickman upper bound is even higher. By comparing Figs. 14 and 16, it can be seen that points A-C in Fig. 16 are well within the confidence interval of the Young's modulus at volume fraction 75% in Fig. 14, obtained with 5 realizations of the RUC.

The volume fraction increases significantly - to 79% - if particles are connected with joints of radius 42.9 μm . The Young's modulus corresponding to such a volume fraction (point E in Fig. 16) turns out to be 28.3 GPa and fits well the experimental data at volume fraction 80%. This may signify that although the surface area increased and large joints have been added, the underlying micro-structural behavior is still captured well. The network of intergranular contacts in Fig. 15 appears to be of less point-wise nature and may correspond to large localized plastic deformations that occurred since rearrangements are no longer possible. Similar conclusions can be drawn for joints with radius 47.9 μm and 52.5 μm (points F,G in Fig. 16), even though it could be argued that the higher the plastic deformation, the less accurate it is to approximate the network of inter-granular contacts with large joints.

Analyses of compounds at different volume fractions - A similar approach was taken on the RUC at volume fraction 70%, see Table 2. In this case, the enlargement of the joints leads to a total 75% volume fraction (point H in Fig. 16) that is higher than analysis for the small joints in Table 1. We may speculate that: i) the underlying micro-structural behavior is not captured well, since large local deformations have been reproduced in place of further rearrangement; ii) the underlying micro-structural behavior is well captured and further rearrangements did not take place in spite of the fact that they were possible, potentially because of very high local friction; iii) both mechanisms would likely take place concurrently. The last statement appears to be the most logical, and may also justify the scatter and the large error bars in the experimental

data. In fact, depending on the non-unique history of rearrangements and deformations, the Young's modulus values may differ significantly.

It was not possible to construct RUCs with volume fractions above 75% due to geometric constraints in the packing algorithm. Packing limitation beyond such a threshold suggests that higher densities can be achieved only with large plastic deformations of grains, which in turn change the interconnecting network from pointwise to a more extensive contact. In other terms, intense irreversible particle sliding and rearrangement may initially occur with limited plastic deformations at point of contact, whereby energy is mainly dissipated due to the inter-particle friction (Poquillon et al., 2002b). Aluminum powders with the morphology of Fig. 7 might reach a 75% volume fraction in this stage. Fig. 1 shows a different trend for powder densification right at such a value. Other publications infer this limit for aluminum powders at 72.5% (Lee and Kim, 2002). A similar behavior has been observed in other metal powder compounds, described in terms of *force-chains* (Makse et al., 2000) with comparable compaction pressures (Poquillon et al., 2002b). Above this threshold, the ability of further compaction is highly dependent upon the inclination of the grains to deform plastically, since particle interlocking triggers further massive plastic deformations. These quantitatively different responses have been observed for different materials in Poquillon et al. (2002b).

The experiments of Carnavas and Page (Carnavas and Page, 1998) concluded that the load response of heavily compressed material is similar to that of a porous solid, i.e. with large contact areas between particles. The analyses in this paper support this conclusion. The increment of Young's modulus is micro-mechanically related to the broadening of the micro-structural interconnecting network during the compaction, which allows the stress percolation paths to widen. Ideally, at complete particle deformation, the contact between grains becomes perfect and *homogeneous* material behavior should be recovered. This effect is made clear in Fig. 17. It plots the percolation paths for the diagonal component σ_{yy} of the Cauchy stress tensor in the loading direction at different volume fractions. The interconnected network of "black" finite elements, capable of transmitting an amount of stress higher than the volume average stress on the RUC, widens with the increase of volume fraction. This outcome agrees well with the evolution of percolating chains in spherical compounds observed in Makse et al. (2000).

The computational domain was built via small spherical joints connecting the random aggregate. As stated, this approach simulates a particle rearrangement with point-wise inter-particle force transmission, and since it allows a transfer of shear forces at the junctions without limitation in magnitude, it is qualitatively equivalent to a partial sintering. Experimental results of Young's modulus of partially sintered alumina particles are available in the literature (see e.g. Green et al., 1988). Outcomes of Fig. 16 can be compared with Fig. 9 in Jefferson et al. (2002) and with Fig. 7 in Green et al. (1988) if sintering is assumed to have taken place at initial packing densities 65%, 70%, and 75% before further compaction. Such a comparison has been done in Fig. 18. Experimental

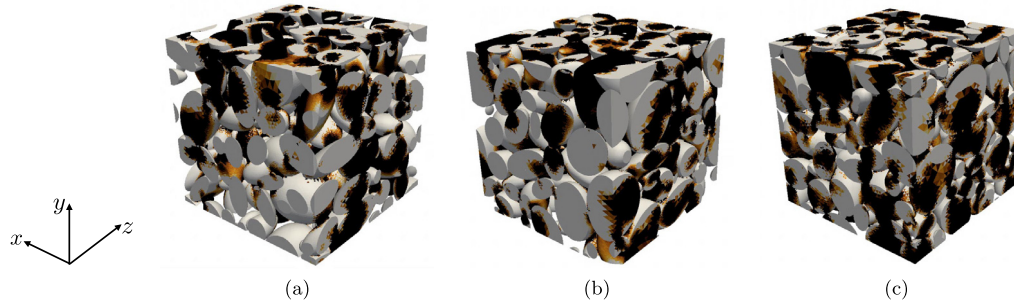


Fig. 17. Stress percolation paths in the RUCs at 65% volume fraction (a), 70% (b), and 75% (c) described in Fig. 13. In the elements painted in black the magnitude of the Cauchy stress, σ_{yy} , in the loading direction is larger than the average stress in the same direction. The gray colored elements have a level of Cauchy stress in the direction of the load less the 50% of the average Cauchy stress in the same direction.

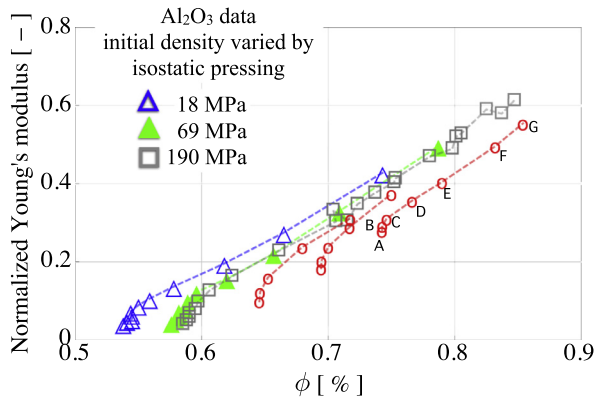


Fig. 18. Experimental data of the effective Young's modulus of a partly sintered ceramic powder (filled and unfilled triangles, unfilled squares) compared with numerical outcomes (circular empty markers). Experimental results are taken from literature (Jefferson et al., 2002; Green et al., 1988). Numerical outcomes are the same as in Fig. 16, normalized by the intrinsic aluminum Young's modulus (70 GPa).

data (filled and unfilled triangles, unfilled squares) refer to the effective Young's modulus of alumina ceramic powders, normalized with the intrinsic, or fully dense, Young's modulus. They have been taken from Fig. 9 in Jefferson et al. (2002). Our predictions on aluminum powders, normalized by the solid aluminum Young's modulus (70 GPa), are plotted with the same notation of Fig. 16. A comparison shows a remarkable qualitative agreement between the numerical solutions and experimental evidence. These simulations are more accurate than the theoretical investigations in Jefferson et al. (2002). The literature values for the intrinsic Young's modulus of alumina are about 300 GPa, i.e. Al_2O_3 is more than four times stiffer than Al. Fig. 18 thus suggests that the evolution of the normalized Young's modulus with the compaction in the volume fractions range of Fig. 18 is not significantly influenced by the intrinsic Young's modulus, but is rather dictated by the evolution of the microstructure. This is compatible with moderate plastic deformations, whereby at higher TMDs the different plastic behavior of alumina (brittle) and aluminum is expected to play a major role.

Anisotropic behavior - It has been clarified here that the behavior more closely resembles a porous solid for higher volume fraction samples, and the variation of the force transmission network becomes lower. This is also indicated by convergence to the boolean model of spheres (see Fig. 16). At small volume fractions though, the percolation paths may differ significantly within the RUC. As a consequence, the response of the RUC may become anisotropic. Table 3 collects the values of computed Young's modulus in the three principal directions of the RUC for a single realization at different volume fractions. The coefficient of variation

(Co.V.) that measures anisotropy decreases significantly as the volume fraction increases.

5. Scaling law

An attempt was made to derive a scaling law between the surface area of the interconnections and the Young's modulus. To this aim, denote with $\bar{E} \geq 1$ the Young's modulus normalized by the smallest estimated one, denoted with E_0 henceforth, with a joint radius of 5.9 μm . Denote with $\bar{A} \geq 0$ the percentage surface area of the interconnections normalized by the total surface area of the particles. Finally, denote with ϕ_0 the volume fraction of the RUC at E_0 . In Table 1, $\phi_0 = 0.742$ (75% RUC) and in Table 2, $\phi_0 = 0.694$ (70% RUC). A scaling law of type

$$\bar{E}(\phi_0, \bar{A}) = \alpha(\phi_0) \sqrt{\bar{A}} \quad (6)$$

was found with parameter $\alpha(\phi_0) \geq 1$. When $\bar{A} \rightarrow 0$ the Young's modulus converges to E_0 , i.e. $\bar{E} \rightarrow 1$, with a square-root asymptotical behavior. Away from ϕ_0 , high order terms dominate.

Fig. 19(a) depicts the scaling law (6) at ϕ_0 65%, 70%, and 75%, and compares it with the data taken from simulations - see columns 5–8 in Tables 1 and 2 for ϕ_0 70% and 75%. Parameter $\alpha(\phi_0)$ has been estimated by a piecewise linear interpolation, noting that $\alpha \rightarrow 1$ when $\phi_0 \rightarrow 1$. A lower estimate $E_0(\phi_0)$ of the Young's modulus at the origin (i.e. small joint approximation) can be extracted from the scaling law (6). To this aim, the normalized surface area \bar{A} when the Young's modulus equals the solid aluminum one (70 GPa) is evaluated first. It is termed $\bar{A}_{70}(\phi_0)$ and plotted in Fig. 20(a). The lower estimate on the Young's modulus follows from the equation

$$E_0(\phi_0) = \frac{70}{\alpha(\phi_0) \sqrt{\bar{A}_{70}(\phi_0)}}. \quad (7)$$

This estimate has been plotted in Fig. 20(b). The trend of the experimental data is captured accurately.

The surface area that has been formed in a compaction process is very influential on several material properties, such as thermal and electrical conductivities. Unfortunately, this important parameter is particularly difficult to measure. An estimate of the surface area can be recovered from the scaling law (6) as a function of the Young's modulus, which in contrast can be measured with well established experiments.

The discrete volume fraction (ϕ) in column 7 of Tables 1 and 2 is the initial volume fraction (ϕ_0) incremented by the volume of the joints. The increase of the volume also leads to an increment in the surface area \bar{A} , printed in column 5 of the same tables. It turns out that $\phi - \phi_0$ and the increment of the area \bar{A} can be approximated well with a linear relation

$$\bar{A} = k(\phi - \phi_0), \quad (8)$$

Table 3
Values of computed Young’s modulus (E) in the three principal directions of the RUC of Fig. 17 for a single realization at different volume fractions.

ϕ [%]	Young’s modulus [MPa]			Mean [MPa]	st. dev. [MPa]	Co. V. [-]
	E_x	E_y	E_z			
50	3730	5155	4222	4369	723	0.165
60	9698	11,723	9907	10,443	1113	0.106
65	12,198	11,587	12,267	12,017	374	0.0311
70	14,885	15,990	15,278	15,384	560	0.0364
75	21,251	20,732	19,711	20,565	783	0.0381

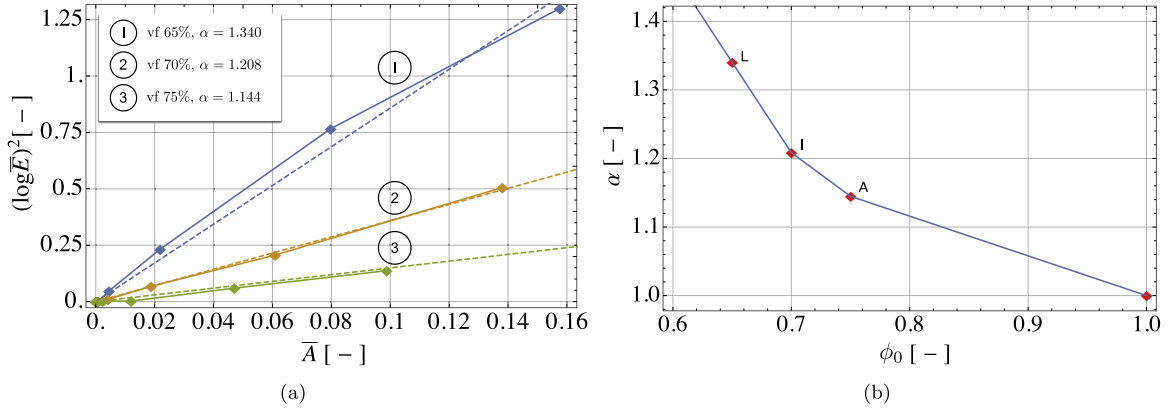


Fig. 19. (a) Scaling laws at 65%, 70%, and 75% volume fraction (dashed lines). Solid lines represent data taken from simulations - see columns 5–8 in Tables 1 and 2 for ϕ_0 70% and 75%. (b) Piecewise linear interpolation of function $\alpha(\phi_0)$. Markers A, I, L in (b) represent the same data points as in Fig. 16.

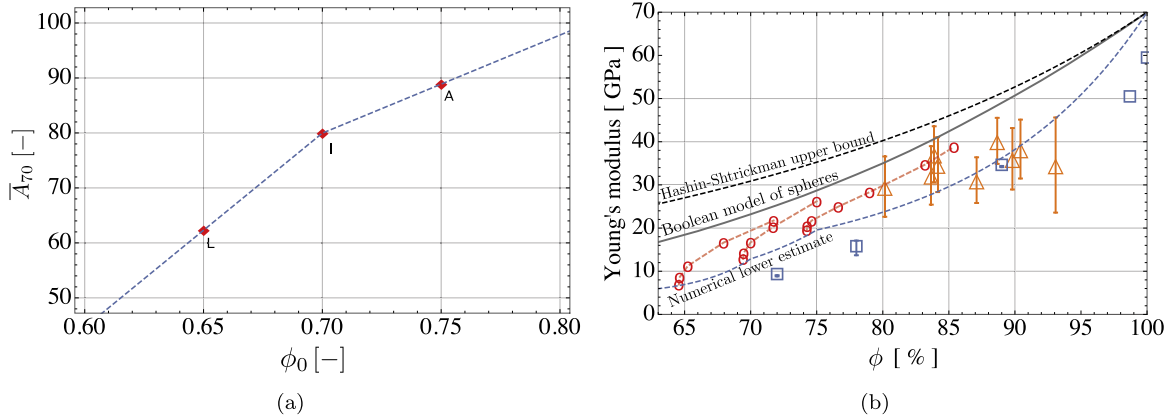


Fig. 20. (a) Piecewise linear interpolation function $\bar{A}_{70}(\phi_0)$. Markers A, I, L represent the same data points as in Fig. 16. (b) The numerical lower estimate curve derived from Eq. (7).

in the neighborhood of ϕ_0 , as seen in Fig. 21(a) with $k = 214.17$. By coupling the scaling law (6) with the lower estimate (7) and the linear expansion (8), the Young’s modulus can be estimated as a function of ϕ and ϕ_0 in the neighborhood of ϕ_0 :

$$E(\phi_0, \phi) = E_0(\phi_0) \alpha(\phi_0) \sqrt{k(\phi - \phi_0)}. \tag{9}$$

This estimate of the Young’s modulus is plotted in Fig. 21(b) against the numerical data already presented in Fig. 16, showing overall good accuracy.

Scaling law (9) can be conveniently used to obtain information on the surface area that has been formed in a compaction process. An example can illustrate this idea well. Assume to have a pack with initial volume fraction $\phi_0=67\%$ (point O in Fig. 22), and to have measured a Young’s modulus of 27 GPa after compaction at a final 80% volume fraction (point M in Fig. 22). Since 27 GPa is larger than the estimate $E_0(0.8)$ (point N in Fig. 22 obtained from Eq. (7)), the compaction process must have involved particle rearrangement and deformation concurrently. If one could ideally plot

the sequence of points $\{\phi, E\}$ during compaction, such a history curve would lie between the two continuous curves $E(0.67, \phi)$ and $E(0.76, \phi)$, within points M, Q, O, P in the shadowed area in Fig. 22. A mere rearrangement from 67% to 76% along the curve E_0 from points O and Q, and sole deformation afterwards, would follow the deformation curve $E(0.76, \phi)$ from point Q to point M. Since a pure deformation from a volume fraction higher than 76% would cause a Young’s modulus between points M and N, one may argue that no mere rearrangement above point Q has taken place. On the other hand, the curve $E(0.67, \phi)$ is the history path taken by pure deformation from point O at $\phi_0=67\%$, which largely overestimates the measured value of the Young’s modulus at $\phi = 0.80$ (point R). Point P that corresponds to Young’s modulus of 27 GPa has $\phi = 0.767$. The surface area increase is limited by the surface area created up to point P. The increment of the surface area can be estimated via Eq. (8) for $\phi_0 = 67\%$, $\phi_0 = 76\%$. If the compaction follows the curve $E(0.67, \phi)$, one has $\bar{A} = 20.77$, whereas

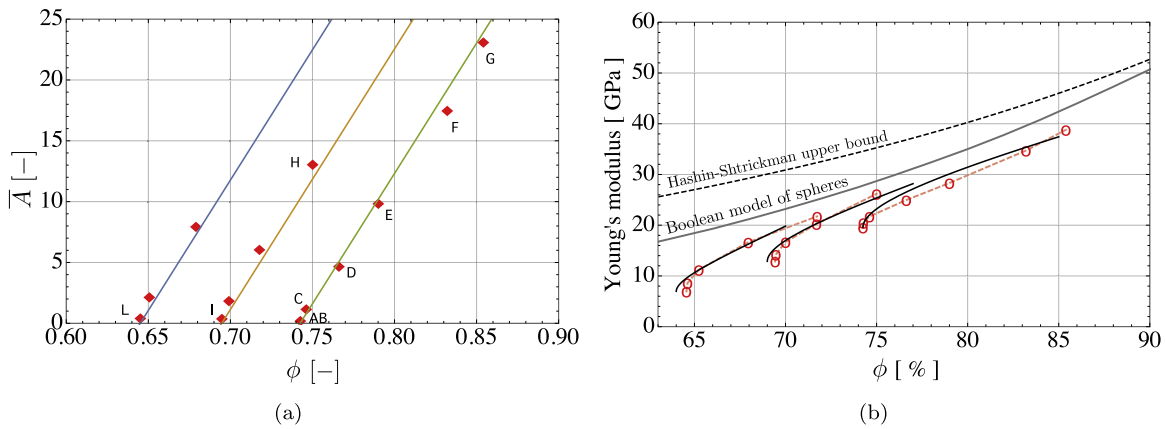


Fig. 21. (a) Linear approximation function $\bar{A}(\phi)$ in the neighborhood of ϕ_0 . Markers A to L represent the same data points as in Fig. 16. (b) Black solids lines correspond to the estimate of the Young's modulus derived from Eq. (9).

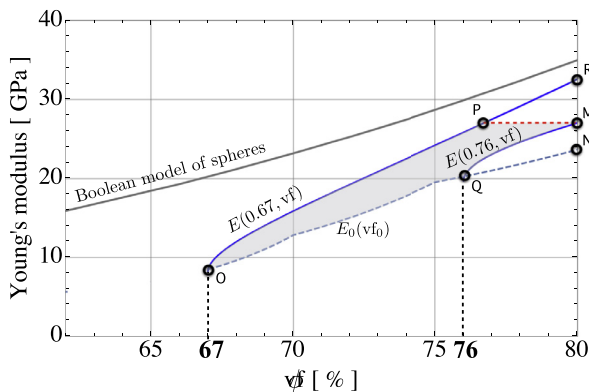


Fig. 22. An illustrative example of the surface area estimate after a compaction process: the increment of surface area can be easily estimated via Eq. (8) for $\phi = 80\%$ and $\phi_0 = 67\%$ and $\phi_0 = 76\%$, respectively.

if the compaction follows the curve $E(0.76, \phi)$, one has $\bar{A} = 8.57$. The packing software provided a total surface area of the particles equal to 14.026 mm^2 and 14.169 mm^2 for $\phi_0 = 67\%$ and $\phi_0 = 76\%$, respectively. Accordingly, the surface area that has been formed in the compaction process is estimated between 1.21 mm^2 and 2.91 mm^2 , respectively.

6. Conclusions and final remarks

In this paper, the Young's modulus of cold compacted metal powders has been estimated via computational simulations, using image-based morphological reconstructions of the microstructure and high performance computing. Computational simulations have been compared with co-designed experimental investigations for the quasi-static Young's modulus. The dynamic Young's modulus was measured, also. Proposed numerical procedures are general and provided insightful comparisons with the Young's modulus of alumina cold compacted powder compounds.

Penetrating conclusions on the micro-mechanics of cold compaction processes have been drawn. As already envisaged on an experimental basis, the load response of moderately compressed powders is dominated by its particulate nature and inter-particle forces, while the load response of heavily compressed material is similar to that of a porous solid. Numerical analysis has shown that, especially at low volume fractions, the two mechanisms of powder compaction (rearrangement and deformation) interact strongly, and a unique value of Young's modulus can hardly be established as a function of the volume fraction only, because it de-

pends on the history of deformation and of the stress percolation path. The importance of the inter-particle morphology and the surface area of such a network has been highlighted and quantified via a novel scaling law. Evidence of anisotropy at low volume fractions, as well as significant scatter in experimental investigations, also confirm this conclusion.

In the current implementation, local tensile states are utterly transmitted by joints, inducing a local cohesion with no magnitude limitation. Moreover, it was not possible to estimate the dynamic Young's modulus numerically without tracking the contact regions between the particles. Further developments may numerically resolve the contact between particles, imposing pure unilateral constraints.

Acknowledgments

We gratefully acknowledge A. Justice for his help in experimental investigations. This work was supported by the Department of Energy, National Nuclear Security Administration, under the award number DE-NA0002377 as part of the Predictive Science Academic Alliance Program II. M. T. Beason was also supported by the Department of Defense (DoD) through the National Defense Science & Engineering Graduate Fellowship (NDSEG) Program. We also acknowledge computational resources from the 2016 ASCR Leadership Computing Challenge (ALCC). Finally, we acknowledge the reviewers for useful comments that improved this paper.

Appendix A. Young's modulus for high energy ball milled Al powder

A second set of measurements was carried out on high energy ball milled Al powders. The initial powders were 99.8% pure Al with -325 mesh size purchased from Alfa Aesar. The powders were ball milled in a Retsch PM100 planetary mill with 10 min (min) active milling time, where each 5 min milling period was followed by a 15 min rest period. The total mass of the powder was 33 g and a crash ratio of 5:1 was used with 440C stainless steel media with a diameter of 6.35 mm. Hexane (20 mL) was included as a process control agent. The rotation speed was 650 rpm (rpm). The powders were dried in air and then sieved using a sieve shaker to a particle size range of 106–355 μm over 24 h.

Fig. A.23 depicts the Young's modulus estimated from experimental measurements. Due to the small displacements at high loading the uncertainty is large. The uniaxial stress experiments show that the elastic response in the 80–90% TMD range for unmilled and milled powders are on the same order. The Young's modulus increases gradually until approximately 95% TMD. After

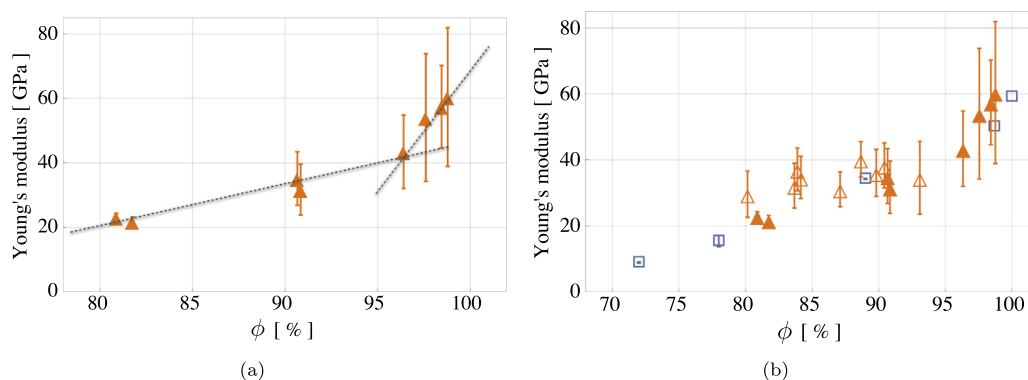


Fig. A1. Young's modulus obtained from experimental measurements: a) high energy ball milled aluminum; b) summary - milled aluminum (filled triangles) powder compounds have been measured quasi-statically, whereas unmilled compounds have been measured quasi-statically (unfilled triangles) as well as dynamically (squares). Error bars represent twice the standard deviation.

this point the modulus increases rapidly, approaching the response of a nonporous solid.

References

- Argani, L., Misseroni, D., Piccolroaz, A., Capuani, D., Bigoni, D., 2016. Plastically-driven variation of elastic stiffness in green bodies during powder compaction. part II: micromechanical modelling. *J. Eur. Ceram. Soc.* 36, 2169–2174.
- Argani, L., Misseroni, D., Piccolroaz, A., Vinco, Z., Capuani, D., Bigoni, D., 2016. Plastically-driven variation of elastic stiffness in green bodies during powder compaction. part I: experiments and elastoplastic coupling. *J. Eur. Ceram. Soc.* 36, 2159–2167.
- Carnavas, P., Page, N., 1998. Elastic properties of compacted metal powders. *J. Mater. Sci. C* 33, 4647–4655.
- Collins, B., Matouš, K., Rypl, D., 2010. Three-dimensional reconstruction of statistically optimal unit cells of multimodal particulate composites. *Int. J. Multiscale Com.* 8 (5), 489–507.
- Doll, S., Schweizerhof, K., 2000. On the development of volumetric strain energy functions. *ASME J. Appl. Mech.* 67, 17–21.
- ASTM Standard E1876-01, 2002. Standard test method for dynamic Young's modulus, shear modulus, and Poisson's ratio by impulse excitation of vibration.
- Fleck, N., 1995. On the cold compaction of powders. *J. Mech. Phys. Solids* 43 (9), 1409–1431.
- Amadio, G., 2014. Particle packings and microstructure modeling of energetic materials. University of Illinois at Urbana-Champaign Ph.D. thesis.
- Gillman, A., Amadio, G., Matouš, K., Jackson, T., 2015. Third-order thermo-mechanical properties for packs of platonic solids using statistical micromechanics. *Proc. R. Soc. A* 471.
- Gillman, A., Matouš, K., 2014. Third-order model of thermal conductivity for random polydisperse particulate materials using well-resolved statistical descriptions from tomography. *Phys. Lett. A* 378 (41), 3070–3073.
- Gillman, A., Matouš, K., Atkinson, S., 2013. Microstructure-statistic-property relations of anisotropic polydisperse particulate composites using tomography. *Phys. Rev. E* 87, 022208.
- Gonzalez, M., Cuitiño, A., 2016. Microstructure evolution of compressible granular systems under large deformations. *J. Mech. Phys. Solids* 93, 44–56. Special Issue in honor of Michael Ortiz. doi: 10.1016/j.jmps.2016.03.024.
- Green, D., Brezny, R., Nader, C., 1988. The elastic behavior of partially-sintered materials. In: *Symposium F – Adhesions in Solids*, volume 119 of MRS Proceedings, pp. 43–49.
- Gu, C., Kim, M., Anand, L., 2001. Constitutive equations for metal powders: application to powder forming processes. *Int. J. Plast.* 17, 147–209.
- Hashin, Z., Shtrikman, S., 1962. On some variational principles in anisotropic and nonhomogeneous elasticity. *J. Mech. Phys. Solids* 10, 335–342.
- Helte, A., 1995. Fourth-order bounds on the effective bulk and shear moduli of random dispersions of penetrable spheres. *Proc. R. Soc. A* 450 (1940), 651–665.
- Jefferson, G., Haritos, G., McMeeking, R., 2002. The elastic response of a cohesive aggregate - a discrete element model with coupled particle interaction. *J. Mech. Phys. Solids* 50, 2539–2575.
- Kadiri, M., Michrafy, A., Dodds, J., 2005. Pharmaceutical powders compaction: experimental and numerical analysis of the density distribution. *Powder Technol.* 157 (1–3), 176–182. doi:10.1016/j.powtec.2005.05.025.
- Kanatani, K., 1981. A theory of contact force distribution in granular materials. *Powder Technol.* 28, 167–172.
- Kim, K., Cho, J., 2001. A densification model for mixed metal powder under cold compaction. *Int. J. Mech. Sci.* 43, 2929–2946.
- Klinzing, G., Zavaliangos, A., Cunningham, J., Mascaro, T., Winstead, D., 2010. Temperature and density evolution during compaction of a capsule shaped tablet. *COMPUT CHEM ENG* 34 (7), 1082–1091. doi:10.1016/j.compchemeng.2010.04.012.
- Kruyt, N., 2016. On weak and strong contact force networks in granular materials. *Int. J. Solids Struct.* 92–93, 135–140.
- Kruyt, N.P., Antony, S.J., 2007. Force, relative-displacement, and work networks in granular materials subjected to quasistatic deformation. *Phys. Rev. E* 75, 051308. doi:10.1103/PhysRevE.75.051308.
- Lapteva, A., Cysne Barbosa, A., Daudt, N., Bram, M., 2016. Review of the powder metallurgical production of net-shaped titanium implants. *Key. Eng. Mat.* 704, 311–317.
- Lee, H., Brandyberry, M., Tudor, A., Matouš, K., 2009. Three-dimensional reconstruction of statistically optimal unit cells of polydisperse particulate composites from microtomography. *Phys. Rev. E* 80 (6), 061301.
- Lee, H., Gillman, A., Matouš, K., 2011. Computing overall elastic constants of polydisperse particulate composites from microtomographic data. *J. Mech. Phys. Solids* 59, 1838–1857.
- Lee, S., Kim, K., 2002. Densification behavior of aluminum alloy powder under cold compaction. *Int. J. Mech. Sci.* 44, 1295–1308.
- Maggi, F., Stafford, S., Jackson, T., Buckmaster, J., 2008. Nature of packs used in propellant modeling. *Phys. Rev. E* 77, 046107.
- Makse, H., Johnson, D., Schwartz, L., 2000. Packing of compressible granular materials. *Phys. Rev. Lett.* 84 (18), 4160–4163.
- Matouš, K., Geers, M., Kouznetsova, V., Gillman, A., 2017. A review of predictive non-linear theories for multiscale modeling of heterogeneous materials. *J. Comput. Phys.* 330, 192–220. doi:10.1016/j.jcp.2016.10.070.
- Michrafy, A., Ringenbacher, D., Tchoreloff, P., 2002. Modelling the compaction behaviour of powders: application to pharmaceutical powders. *Powder Technol.* 127 (3), 257–266. doi:10.1016/S0032-5910(02)00119-5.
- Milton, G., 2002. *The Theory of Composites*. Cambridge University Press. Cambridge Books Online.
- Mosby, M., Matouš, K., 2015. On mechanics and material length scales of failure in heterogeneous interfaces using a finite strain high performance solver. *Modell. Simul. Mater. Sci. Eng.* 23, 085014.
- Mosby, M., Matouš, K., 2016. Computational homogenization at extreme scales. *Extreme Mech. Lett.* 6, 68–74.
- Pham, D., Torquato, S., 2003. Strong-contrast expansions and approximations for the effective conductivity of isotropic multiphase composites. *J. Appl. Phys.* 94 (10), 6591–6602.
- Piccolroaz, A., Bigoni, D., Gajo, A., 2006. An elastoplastic framework for granular materials becoming cohesive through mechanical densification. Part I - small strain formulation. *Eur. J. Mech. A-Solid* 25 (2), 334–357. doi:10.1016/j.euromechsol.2005.10.001.
- Piccolroaz, A., Bigoni, D., Gajo, A., 2006. An elastoplastic framework for granular materials becoming cohesive through mechanical densification. Part II - the formulation of elastoplastic coupling at large strain. *Eur. J. Mech. A-Solid* 25 (2), 358–369. doi:10.1016/j.euromechsol.2005.10.002.
- Poquillon, D., Baco-Carles, V., Tailhades, P., Andrieu, E., 2002. Cold compaction of iron powders - relations between powder morphology and mechanical properties. Part I. bending tests: results and analysis. *Powder Technol.* 75–84.
- Poquillon, D., Lemaître, J., Baco-Carles, V., Tailhades, P., Lacaze, J., 2002. Cold compaction of iron powders - relations between powder morphology and mechanical properties. Part I: powder preparation and compaction. *Powder Technol.* 65–74.
- Radjai, F., Wolf, D., Jean, M., Moreau, J., 1998. Bimodal character of stress transmission in granular packings. *Phys. Rev. Lett.* 80, 61–64. doi:10.1103/PhysRevLett.80.61.
- Roberts, A., Garboczi, E.J., 2002. Computation of the linear elastic properties of random porous materials with a wide variety of microstructure. *Proc. R. Soc. A* 458 (2021), 1033–1054.
- Serra, J., 1980. The boolean model and random sets. *Comput. Vision Graph* 12 (2), 99–126.
- Shuck, C., Frazee, M., Gillman, A., Beason, M.T., Gunduz, I., Matouš, K., Winarski, R., Mukasyan, A.S., 2016. X-Ray nanotomography and focused-ion-beam sectioning for quantitative three-dimensional analysis of nanocomposites. *J. Synchrotron Radiat.* 23 (4), 990–996. doi:10.1107/S1600577516007992.

- Stafford, D., Jackson, T., 2010. Using level sets for creating virtual random packs of nonspherical convex shapes. *J. Comput. Phys.* 229, 3295–3315.
- Stoyan, D., Mecke, K., 2005. The boolean model: from Matheron till today. In: Bilodeau, M., Meyer, F., Schmitt, M. (Eds.), *Space, Structure and Randomness: Contributions in Honor of Georges Matheron in the Field of Geostatistics, Random Sets and Mathematical Morphology*. Springer New York, New York, NY, pp. 151–181. doi:10.1007/0-387-29115-6_8.
- Torquato, S., 1997. Effective stiffness tensor of composite media: I. Exact series expansions. *J. Mech. Phys. Solids* 45 (9), 1421–1448.
- Torquato, S., 1998. Effective stiffness tensor of composite media: II. Applications to isotropic dispersions. *J. Mech. Phys. Solids* 46 (8), 1411–1440.
- Torquato, S., 2002. *Random Heterogeneous Materials: Microstructure and Macroscopic Properties*. Springer.
- Wang, J., Qu, X., Yin, H., Yi, M., Yuan, X., 2009. High velocity compaction of ferrous powder. *Powder Technol.* 192, 131–136.
- Wu, C.-Y., Ruddy, O., Bentham, A., Hancock, B., Best, S., Elliott, J., 2005. Modelling the mechanical behaviour of pharmaceutical powders during compaction. *Powder Technol.* 152 (1–3), 107–117. doi:10.1016/j.powtec.2005.01.010.